Depth-Resolved Measurements of the Meissner Screening Profile in Surface-Treated Nb

Ryan M. L. McFadden,[1,2,*] Md. Asaduzzaman,[1,2] Thomas Prokscha,[3] Zaher Salman,[3] Andreas Suter,[3] and Tobias Junginger[1,2,†]

[1] *TRIUMF, 4004 Wesbrook Mall, Vancouver, British Columbia V6T 2A3, Canada*
[2] *Department of Physics and Astronomy, University of Victoria, 3800 Finnerty Road, Victoria, British Columbia V8P 5C2, Canada*
[3] *Laboratory for Muon Spin Spectroscopy, Paul Scherrer Institute, Forschungsstrasse 111, 5232 Villigen, Switzerland*

(Received 22 December 2022; accepted 28 February 2023; published 6 April 2023)

We report depth-resolved measurements of the Meissner screening profile in several surface-treated Nb samples using low-energy muon spin rotation. In these experiments, implanted positive muons, whose stopping depths below Nb's surface are adjusted between approximately 10 nm and 150 nm, reveal the field distribution inside the superconducting element via their spin precession (communicated through their radioactive decay products). We compare how the field screening is modified by different surface treatments commonly used to prepare superconducting radio-frequency cavities used in accelerator beamlines. In contrast to an earlier report [A. Romanenko *et al.*, Appl. Phys. Lett. **104**, 072601 (2014)], we find no evidence for any "anomalous" modifications to the Meissner profiles, with all data being well described by a London model. Differences in screening properties between surface treatments can be explained by changes to the carrier mean free paths resulting from dopant profiles near the material's surface.

DOI: 10.1103/PhysRevApplied.19.044018

I. INTRODUCTION

Since its discovery in the early 19th century, the elemental metal Nb has been the subject of intense study, culminating in a detailed understanding of its chemical properties (see, e.g., Refs. [1–3]). Of equal (if not greater) interest are the element's electronic properties, especially those relating to its superconductivity. For example, while Nb is one of the many superconducting elements [4], its transition temperature $T_c \approx 9.25$ K is the highest among them at ambient pressure. Accompanying this accolade is a lower critical field $B_{c1} \approx 170$ mT that exceeds the critical field of all other (type-II) superconductors, making the element particularly suited for devices that must remain flux-free under modest magnetic fields. These intrigues inspired comprehensive measurements [5–8] and calculations [9–14] relating to its electronic structure, as well as how it is modified under pressure [15]. This, in turn, has led to a thorough understanding of its superconductivity [16–18], including details such as its "strong" [19] electron-phonon coupling [20–22], nonlocal electrodynamics [23,24] in "clean" samples [25], and vortex lattice structure [26–28]. This high degree of understanding has prompted Nb's frequent use in complex heterostructures where a superconducting layer is required (see, e.g., Refs. [29–38]). These physical traits, in conjunction with the metal's mechanical properties [39,40], have also made Nb particularly suited for use in superconducting radio-frequency (SRF) cavities [41–43], which use a large electric field, E_{acc}, to accelerate charged particles in accelerator beamlines. Of particular importance for this application is the maximum achievable value for E_{acc}, which is fundamentally limited by Nb's ability to expel magnetic flux (i.e., to remain in the Meissner state). This application, in particular, has been a driving factor in the continued refinement of our understanding of the element.

Central to Nb's performance in SRF cavities is the preparation of its surface, with many empirical "recipes" developed (e.g., low-temperature baking [44], two-step baking [45], nitrogen doping [46], and nitrogen infusion [47]) explicitly to boost cavity performance (i.e., maximizing its quality factor Q for the largest possible range of E_{acc}). While it has long been known that surfaces play an important role in determining the field of first flux entry (see, e.g., Ref. [48]), some significant progress has been made recently. For example, it has been demonstrated that Nb can expel flux up to its so-called superheating field B_{sh} (see, e.g., Ref. [49]) by coating it with a thin superconducting film [50], with

*rmlm@triumf.ca
†junginger@uvic.ca

sample geometry and surface preparations also playing an important role [51]. For the latter, the effect can be subtle for samples with identical geometries [52]; however, measurements of their Meissner screening profiles revealed significant differences between select treatments [53], with low-temperature baking [44] postulated as creating an "effective" superconductor-superconductor bilayer [54–56] near the surface (i.e., from a thin region of "dirty" Nb near the surface on top of the "clean" bulk). While this has stimulated renewed interest in using multilayers for SRF applications, the results are controversial and warrant further investigation.

Currently, there are relatively few experimental techniques with the right combination of electromagnetic and spatial sensitivity to achieve this goal (e.g., ion-implanted β-detected nuclear magnetic resonance (NMR) [57,58] and LE-μSR [59–61]). One possibility is to use LE-μSR [59,61], which uses muons implanted in the near-surface region (depths less than approximately 150 nm) as local "magnetometers." This technique has been used to study Meissner screening in Nb with success, revealing the importance of nonlocal electrodynamics [23,24] and strong-coupling corrections [19] in "clean" samples [25], the impact of growth methods on the screening properties of Nb/Cu films used in SRF cavities [62], and the aforementioned "anomalous" modification in the character of the screening profile by mild baking [53]. To clarify the origin of the latter, here we use LE-μSR to quantify the screening profile in Nb samples with surface treatments commonly used in SRF applications [44,45,47]. Our results reveal no "anomalous" modifications to the screening profiles for *any* of the surface treatments, with all profiles being well described by a London model [63]. The surface treatments are found to produce different magnetic penetrations depths, which can be explained by dissimilar carrier mean free paths within the first 150 nm below the surface.

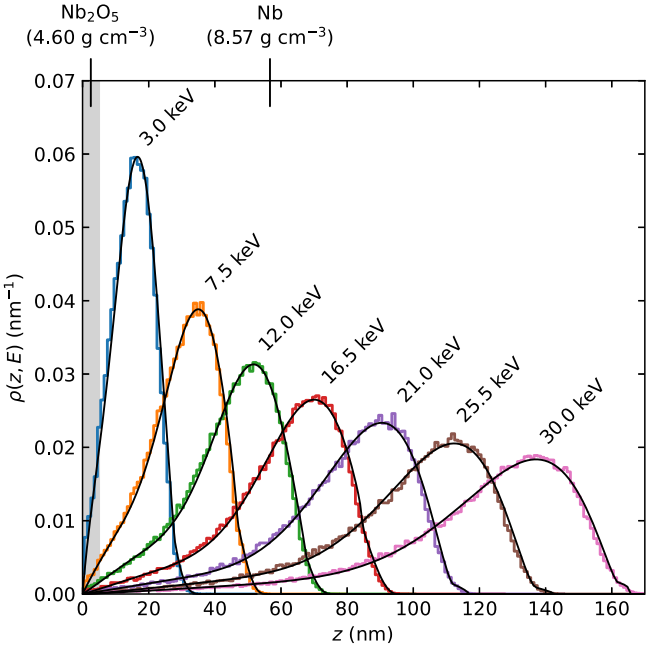

FIG. 1. Typical stopping profiles $\rho(z,E)$ for μ^+ implanted in a Nb_2O_5(5 nm)/Nb target at different energies E (indicated in the inset), simulated using the Monte Carlo code TRIM.SP [70–72]. The profiles, represented as histograms with 1-nm bins, are generated from 10^5 projectiles. The solid black lines denote fits to a model for $\rho(z,E)$ [Eqs. (14) and (15)—see Sec. III], clearly capturing all features of the individual profiles. Additional simulation details can be found in the Appendix.

II. EXPERIMENTAL DETAILS

A. LE-μSR experiments

LE-μSR experiments are performed at the Paul Sherrer Institute's Swiss Muon Source (located in Villigen, Switzerland). Using the $\mu E4$ beamline [64], we generate "low-energy" muons by moderating the energy of an approximately-4-MeV "surface" muon beam using a film of condensed cryogenic gas [65,66] and electrostatically reaccelerating the eluted epithermal (approximately-15-eV) muons to energies on the order of 15 keV. The resulting beam, with a typical intensity of approximately 10^4 s^{-1}, is delivered to a dedicated spectrometer [64,67,68] using electrostatic optics housed within an ultrahigh-vacuum beamline. The μ^+ arrival times are triggered on a thin (approximately-10-nm) carbon-foil detector, causing a slight reduction in their mean kinetic energy (approximately 1 keV) and an (asymmetric) energy spread (approximately 450 eV) before they reach the sample. Control over the μ^+ implantation energy is achieved by our biasing an electrically isolated sample holder using a high-voltage power supply, providing access to stopping depths between approximately 10 nm and 150 nm below the sample surface. The stopping of μ^+ in solids can be accurately computed [69] using Monte Carlo codes (e.g., TRIM.SP [70–72]), which we use here to simulate μ^+ stopping profiles in Nb (see Fig. 1). To ensure the accuracy of these predictions, we revise the parameterization of Nb's electronic stopping cross section for protonlike projectiles [73,74] using a Varelas-Biersack fit [75] to an up-to-date compilation [76] of experimental values [77–80]. The revised fit suggests that earlier calculations (see, e.g., Refs. [25,29–38,53,62]) likely underestimate the μ^+ range in Nb (or Nb layers). Further details are given in the Appendix.

The basis of the LE-μSR technique [59–61,81] involves implanting a beam of (approximately 100%) spin-polarized μ^+ particles into a sample of interest and observing their spins, **S**, reorient in their local magnetic field, **B**. This process is monitored via the anisotropic β emissions from μ^+ decay (mean lifetime $\tau_\mu = 2.1969811(22)$ μs

[82]), wherein the direction of the emitted β rays is probabilisitically correlated with **S** at the moment of decay (see, e.g., Ref. [83]). When **B** is transverse to the spin direction, $\langle S \rangle$ will precess at a rate equal to the probe's Larmor frequency:

$$\omega_\mu = \gamma_\mu B, \tag{1}$$

where $\gamma_\mu/2\pi = 135.5388094(30)$ MHz T^{-1} is the muon gyromagnetic ratio [84]. In the experiments reported here, this so-called transverse-field geometry is used (see, e.g., Refs. [59,83]), wherein an external field $B_{\text{applied}} \approx 25$ mT is applied perpendicular to the initial direction of μ^+ spin polarization and parallel to the surface of our Nb samples. This configuration is highly sensitive to inhomogeneities in B (as expected near the surface of a superconductor in the Meissner state), allowing the local field distribution, $p(B)$, to be measured, which reflects the screening properties of the samples.

In our LE-μSR measurements, the temporal evolution of the *asymmetry*, $A(t)$, in the β rates recorded for two opposing detectors (i.e., 180° opposite one another), is monitored after μ^+ implantation. The counts in a single detector, $N_\pm$, are given by

$$N_\pm(t) = N_{0,\pm} \exp\left(-\frac{t}{\tau_\mu}\right)[1 \pm A(t)] + b_\pm, \tag{2}$$

where $N_{0,\pm}$ and $b_\pm$ are denote the incoming rates of "good" and "background" decay events. While Eq. (2) can be rearranged for $A(t)$, in a two-counter experiment it can be determined directly from the normalized difference in β rates from the two counters:

$$A(t) \equiv \frac{[N_+(t) - b_+] - \alpha\,[N_-(t) - b_-]}{[N_+(t) - b_+] + \alpha\,[N_-(t) - b_-]} = A_0 P_\mu(t), \tag{3}$$

where A_0 is a constant whose precise value depends on both the geometry of the experiment and the details of μ^+ decay, and the factor $\alpha \equiv N_{0,+}/N_{0,-}$ accounts for differences between the detector pair (e.g., detection efficiencies and solid-angle coverage [83,85]). The time dependence in Eq. (3) is determined entirely by the spin polarization of the muon ensemble, $P_\mu(t)$, which depends on $p(B)$ according to

$$P_\mu(t) = \int_{-\infty}^{+\infty} p(B)\cos(\omega_\mu t + \phi)\, dB, \tag{4}$$

where t is the time (in microseconds) after implantation and ϕ is a phase factor that depends on the experimental setup (approximately −40° here). Note that Eq. (4) makes the simplifying assumption that $P_\mu(0) \approx 1$ (i.e., the μ^+ particles are initially approximately 100% spin polarized). Thus, from the synergistic information encapsulated within $P_\mu(t)$ and the simulated μ^+ stopping profiles (see Fig. 1), it is feasible to reconstruct how B varies with depth, z, below the sample surface (see below).

B. Samples

In accord with the standard practice used when SRF cavities are fabricated [41–43], all samples were sourced from high-residual-resistivity-ratio Nb (i.e., residual-resistivity ratio of at least 300). Each sample consists of a piece of the "stock" metal machined into a flat plate (approximately 25 mm by 25 mm by 1.5 mm) with a small circular aperture (approximately 6.5 mm diameter) in one corner. The pieces are then hand polished to remove any sharp edges, followed by buffered chemical polishing to remove any damaged layers near the surface (see, e.g., Ref. [86]). Subsequently, the samples are annealed at 1400 °C for 5 h to remove any mechanical stresses remaining in the metal. Afterwards, an additional round of buffered chemical polishing is performed to remove the topmost 10 μm of material from the surface (i.e., to remove any contaminants introduced from the oven during annealing). In the remainder of this article, we denote this as the "baseline" surface treatment for SRF-cavity-grade Nb. This process has been shown to remove virtually all pinning [51].

On top of the "baseline" preparation, several samples undergo additional surface treatments. One sample is baked at 120 °C for 48 h in an ultrahigh vacuum [44], which we call "120 °C bake." Another sample undergoes a two-step baking procedure, wherein it is initially heated to 75 °C for 5 h and then additionally to 120 °C for 48 h [45], which we denote as "75 °C + 120 °C bake." Lastly, one sample is initially heated to 800 °C for 3 h in a high vacuum and is subsequently baked at 120 °C for 48 h in a 25-mTorr N_2 atmosphere [47], which we refer to as "N_2 infusion." A magnetometric characterization of Nb samples with identical surface treatments can be found elsewhere [52].

III. RESULTS AND ANALYSIS

Typical time-differential LE-μSR data for our surface-treated Nb samples are shown in Fig. 2. In the normal state ($T > T_c$), there is no significant energy dependence for the temporal evolution of $A(t)$, indicating that all implanted muons sample the same local field distribution below the sample surface. This is evident from the identical precession frequencies and damping envelopes, the latter being (predominantly) a result of the host ^{93}Nb nuclei [spin $I = 9/2$; $\gamma/2\pi = 10.4523(5)$ MHz T^{-1}; 100% natural abundance] [87]. By contrast, $A(t)$ depends strongly on the implantation energy in the Meissner state. As the implantation energy increases, the μ^+ spin-precession frequency decreases, accompanied by substantial damping of the signal. These features are expected for a broad $p(B)$ whose mean shifts to lower values at increasing depths below

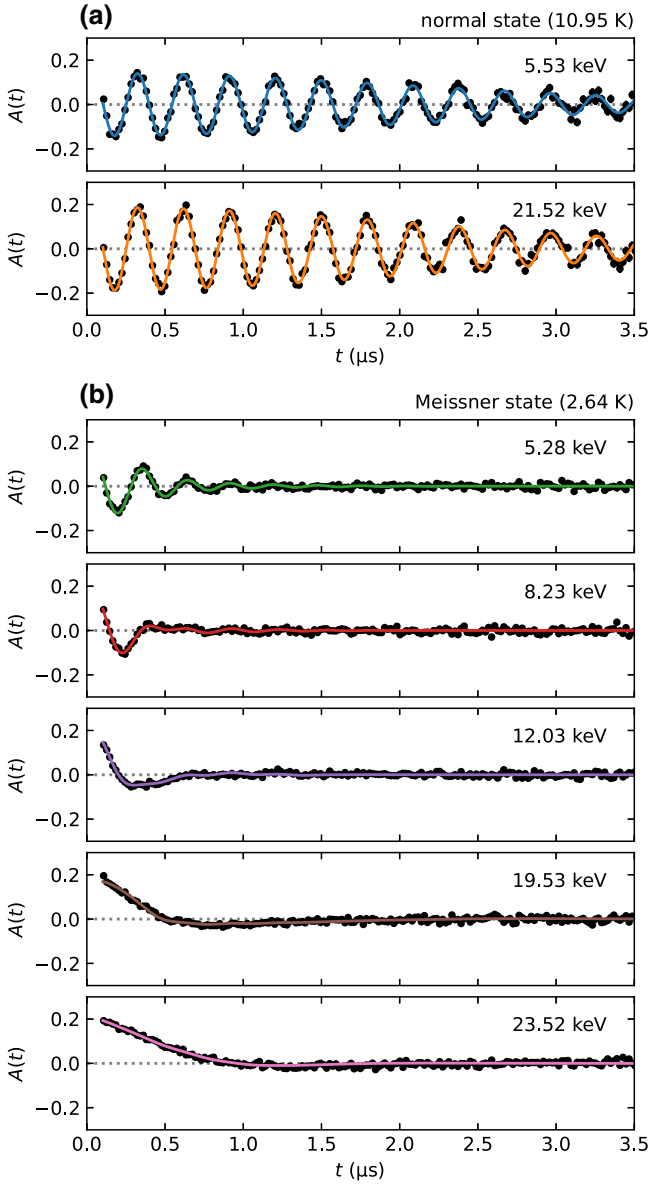

FIG. 2. Implantation-energy dependence of transverse-field LE-μSR data in Nb ("baseline"), measured in both the normal state (11 K) and the Meissner state (2.6 K) with an applied magnetic field of 25 mT. The μ^+ energy E is indicated in the inset of each subplot. In the normal state (a), there is no significant energy dependence for the temporal evolution of $A(t)$, implying that all implanted muons sample the same local field distribution $p(B)$ below the sample surface. By contrast, in Meissner state (b), $A(t)$ depends strongly on the implantation energy. As the implantation energy increases, the μ^+ spin-precession frequency decreases, accompanied by increased damping of the signal, consistent with screening of the magnetic field with increasing depths below the sample surface. The colored lines denote a fit to *all* of the data (i.e., a global fit) using Eqs. (10) and (8)–(6), where the phase ϕ is shared as a common parameter. Clearly, the model captures all of the data's main features. Note that the Gaussian term in Eq. (10) accounts for the small fraction (less than 10%) of muons that do not stop in the sample (e.g., due to backscattering).

the surface, consistent with the expected "signature" for screening of the applied magnetic field.

To quantify these details, we now consider an analysis of the data, which amounts to choosing an (analytic) approximation for the field distribution in Eq. (4). Often, $p(B)$ can be approximated by a Gaussian distribution (see, e.g., Ref. [83]):

$$p_G(B) = \frac{1}{\sqrt{2\pi}}\left(\frac{\gamma_\mu}{\sigma}\right)\exp\left\{-\frac{1}{2}\left[\frac{B-B_0}{(\sigma/\gamma_\mu)}\right]^2\right\}, \qquad (5)$$

where B_0 and σ denote the distribution's location (i.e., mean) and width, respectively. On substitution of Eq. (5) for $p(B)$ into Eq. (4), one gets

$$P_G = \exp\left(-\frac{\sigma^2 t^2}{2}\right)\cos\left(\gamma_\mu B_0 t + \phi\right), \qquad (6)$$

which says that the observed precession frequency is given by the mean of the distribution and that the degree of damping is determined by its width. While this symmetric distribution works well in many instances, the field distribution below the surface of a material in the Meissner state is expected to be intrinsically *asymmetric* (i.e., because the applied field decays to zero inside the material). Therefore, a better approximation for $p(B)$ in our samples is given by a *skewed* Gaussian [88]:

$$p_{\mathrm{SG}}(B) = \sqrt{\frac{2}{\pi}}\left(\frac{\gamma_\mu}{\sigma_- + \sigma_+}\right) \times \begin{cases} \exp\left\{-\frac{1}{2}\left[\frac{B-B_0}{(\sigma_-/\gamma_\mu)}\right]^2\right\} & \text{for } B < B_0, \\ 1 & \text{for } B = B_0, \\ \exp\left\{-\frac{1}{2}\left[\frac{B-B_0}{(\sigma_+/\gamma_\mu)}\right]^2\right\} & \text{for } B > B_0, \end{cases} \qquad (7)$$

where B_0 is the "peak" field (i.e., *not* the mean of the distribution) and σ_+ and σ_- define the distribution's width (i.e., on either side of B_0). Note that the definition in Eq. (7) is somewhat unusual for a skewed Gaussian distribution; it is more commonly defined as

$$p_{\mathrm{SG}}(B) = p_G(B)\left(1 + \mathrm{erf}\left\{\frac{\varsigma}{\sqrt{2}}\left[\frac{B-B_0}{(\sigma/\gamma_\mu)}\right]\right\}\right),$$

where $\mathrm{erf}(z)$ is the error function and $\varsigma \in [-\infty, +\infty]$ is the "skewness" parameter [89]. While this formulation is elegant, the piecewise definition in Eq. (7) has the pragmatic advantage of being amenable to fast computation

during fitting. Specifically, on substituting Eq. (7) for $p(B)$ into Eq. (4), one can write the solution to the integral as [88]

$$P_{\rm SG}(t) = P^{-}_{\rm SG}(t) + P^{+}_{\rm SG}(t), \tag{8}$$

where

$$P^{\pm}_{\rm SG}(t) = \left(\frac{\sigma_{\pm}}{\sigma_{+}+\sigma_{-}}\right)\exp\left(-\frac{\sigma^2_{\pm}t^2}{2}\right) \left[\cos(\gamma_{\mu}B_0 t+\phi) \mp \mathrm{Erfi}\left(\frac{\sigma_{\pm}t}{\sqrt{2}}\right)\sin(\gamma_{\mu}B_0 t+\phi)\right], \tag{9}$$

and Erfi(z) is the complex error function [90]. We find that Eqs. (8) and (9) give the best agreement with the signal in our Nb samples over the full time range of the measurement, without overparamaterization [91].

Returning to our task of fitting the LE-μSR data, explicitly, we use the expression

$$A(t) = A_0\left[fP_{\rm SG}(t) + (1-f)P_G(t)\right], \tag{10}$$

where A_0 is an energy-dependent constant (on the order of approximately 0.2 here), f is the fraction of the signal originating from our sample (typically > 0.9), and the remaining terms, $P_{\rm SG}(t)$ and $P_G(t)$, are given by Eqs. (8) and (9) and Eq. (6), respectively. Additionally, all measurements for a given sample are fit simultaneously (i.e., in a so-called global fit) using a common ϕ. This constraint is necessary, as the phase becomes ill-defined when $A(t)$ is strongly damped and few full precession periods are resolved (e.g., for measurements in the Meissner state at high implantation energies, where the μ^+ stopping depths are far below the surface) [92]. All fitting is performed with MUSRFIT [93], which uses the MINUIT2 minimization routines [94] implemented within the ROOT framework [95]. In all cases, this fitting approach yields excellent agreement with the data (reduced χ^2 of approximately 1.06), and a subset of the results is shown in Fig. 2.

To reconstruct the field profile below the surface, at each implantation energy we identify the mean field sensed by the implanted μ^+ using [88]

$$\langle B\rangle \equiv \int_{-\infty}^{+\infty} B\, p_{\rm SG}(B)\, dB = B_0 + \sqrt{\frac{2}{\pi}}\left(\frac{\sigma_{+}-\sigma_{-}}{\gamma_{\mu}}\right), \tag{11}$$

and the results for each surface treatment are shown in Fig. 3 [96]. As expected, the $\langle B\rangle$ values measured in the normal state are independent of the implantation energy, whereas $\langle B\rangle$ decreases monotonically with increasing E in the Meissner state. It is evident that the screening properties of each surface treatment are different; the applied field is attenuated most strongly for the "baseline" and "75 °C + 120 °C bake" [45] samples, whereas the screening is weaker for the "120 °C bake" treatment [44] and even more so for the "N_2 infusion" treatment [47]. Interestingly, measurements in some of the samples at the lowest E values show that $\langle B\rangle$ plateaus at a value close to the nominal applied field, suggesting the presence of a thin layer near the surface where the external field is not screened (i.e., a so-called "dead layer" at the superconductor's surface). Such a region is fairly generic and is observed in a wide range of superconductors (see, e.g., Refs. [25,53,62,97–103]), although there is considerable variability between materials or even samples (e.g., as a result of surface roughness [104–106]).

To evaluate the magnetic penetration depth λ, it is necessary to construct a model capable of describing the data. The model must account for two crucial details: how the magnetic field is screened below the surface as a function of depth z, and the depth distribution $\rho(z,E)$ sampled by the implanted μ^+. We consider each of these below. Note that while our approach differs somewhat from earlier work in Nb (see, e.g., Refs. [25,53,62]), it is capable of accurately reproducing all measured quantities derived from our experiments.

First, we consider the magnetic field profile, $B(z)$, below Nb's surface. In the simplest case, $B(z)$ decreases exponentially with increasing depth, z, in the Meissner state, as predicted by the London model [63]. Recalling that our data suggest the presence of a "dead layer" at the sample surface, we incorporate this detail *ad hoc* into the London result [63] with the expression (see, e.g., Refs. [97,99])

$$B(z) = \tilde{B}_0 \times \begin{cases} 1 & \text{for } z < d, \\ \exp\left\{-\dfrac{(z-d)}{\lambda}\right\} & \text{for } z \geq d, \end{cases} \tag{12}$$

where λ is the magnetic penetration depth, d is the thickness of the "dead layer" (i.e., where $\tilde{B}_0$ is not screened), and $\tilde{B}_0$ is the (effective) applied magnetic field. The latter quantity is given by

$$\tilde{B}_0 = B_{\rm applied} \times \begin{cases} 1 & \text{for } T > T_c, \\ \left(1-\tilde{N}\right)^{-1} & \text{for } T \ll T_c, \end{cases} \tag{13}$$

where $B_{\rm applied}$ is the applied magnetic field and $\tilde{N}$ is the sample's (effective) demagnetization factor [107]. Note that the inclusion of the factor $(1-\tilde{N})^{-1}$ in Eq. (13) accounts for any apparent "enhancement" of the applied field due to the sample's geometry (i.e., from flux expulsion in the Meissner state—see, e.g., Ref. [108]). Although Eq. (12) is rather simple compared with other models for $B(z)$ (see, e.g., Refs. [23,24]), it sufficiently describes the behavior we observe (see below).

We now consider the μ^+ implantation profiles. As alluded to in Sec. II, the slowing down of implanted μ^+

is a stochastic process, resulting in a *distribution* of stopping depths that can be reliably simulated [69] using Monte Carlo codes such as TRIM.SP [70–72] (see the Appendix for specific details). For our analysis, it is convenient to have the ability to describe these profiles at *arbitrary* E, which is achieved by our fitting of the simulated profiles and interpolating their "shape" parameters. We find that the μ^+ stopping probability, $\rho(z,E)$, at a given E can be described, in general, by

$$\rho(z,E) = \sum_i^n f_i p_i(z), \tag{14}$$

where $p_i(z)$ is a probability density function, $f_i \in [0,1]$ is the ith stopping fraction, constrained such that

$$\sum_i^n f_i \equiv 1,$$

and z is the depth below the surface. For our target (Nb_2O_5(5 nm)/Nb—see, e.g., Ref. [109]), the stopping data are well described with $n = 2$ and a $p(z)$ given by a modified β distribution [110]. Explicitly,

$$p(z) = \begin{cases} 0 & \text{for } z < 0, \\ \dfrac{(z/z_0)^{\alpha-1}\,(1-z/z_0)^{\beta-1}}{z_0\,B(\alpha,\beta)} & \text{for } 0 \le z \le z_0, \\ 0 & \text{for } z > z_0, \end{cases} \tag{15}$$

where $z \in [0, z_0]$ is the depth below the surface and $B(\alpha,\beta)$ is the β function,

$$B(\alpha,\beta) \equiv \frac{\Gamma(\alpha)\Gamma(\beta)}{\Gamma(\alpha+\beta)},$$

with $\Gamma(s)$ denoting the Γ function,

$$\Gamma(s) \equiv \int_0^\infty x^{s-1}\exp(-x)\,dx.$$

Note that the "extra" z_0 in the denominator of Eq. (15) ensures proper normalization of $p(z)$.

To achieve good "coverage" across the range of E values achievable by LE-μSR (approximately 0.5 keV to 30 keV), we simulate μ^+ stopping profiles in small energy increments (500 eV) spanning the entire E range. We then fit each of the simulated stopping profiles using Eqs. (14) and (15) and interpolate the resulting "shape" (i.e., fit) parameters to generate $\rho(z,E)$ at arbitrary E. Results from this procedure are shown in Fig. 1, and are in excellent agreement with the Monte Carlo simulations.

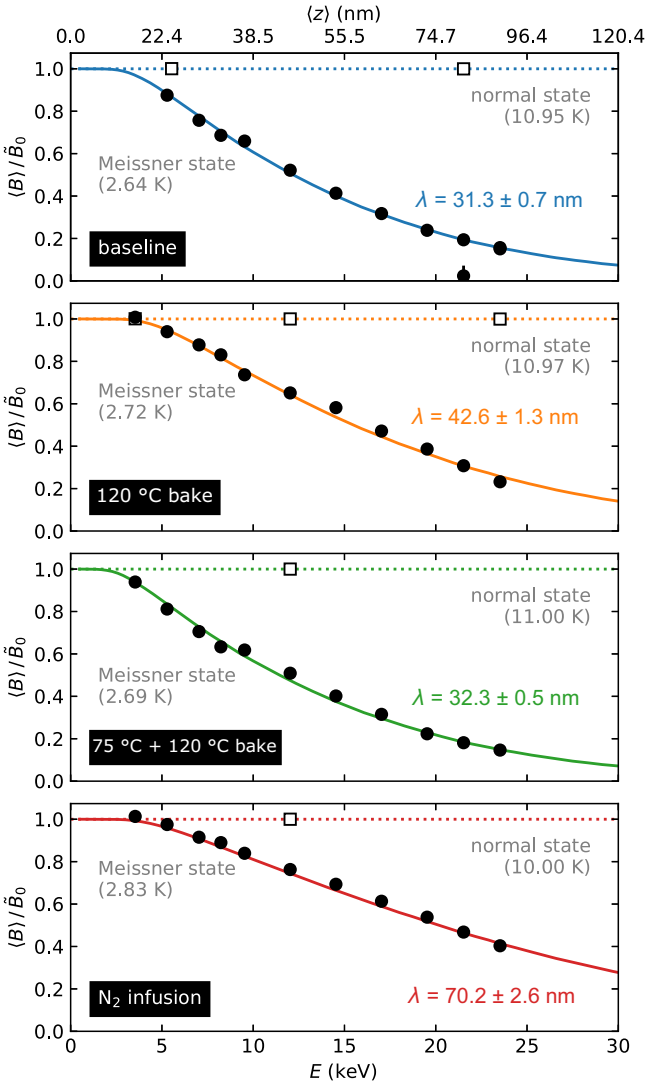

FIG. 3. Mean magnetic field $\langle B\rangle$ (normalized by the "effective" applied field $\tilde{B}_0$) sensed by the implanted μ^+ at different energies E in Nb samples that receive different surface treatments ("baseline," "120 °C bake" [44], "75 °C + 120 °C bake" [45], and "N_2 infusion" [47]—see Sec. II B). For increasing E, the mean μ^+ stopping depth $\langle z\rangle$ increases, covering a length scale comparable to the magnetic penetration depth λ. In the normal state ($T > T_c$), there is no depth dependence of $\langle B\rangle$ for any of the samples, and its value corresponds to the applied magnetic field B_{applied}. Conversely, in the Meissner state (approximately 2.7 K), $\langle B\rangle$ decays rapidly with increasing E above a threshold value, reflecting a small (nonsuperconducting) "dead layer" d at the surface and the increased screening of B_{applied} at deeper depths. The solid and dashed colored lines represent a (global) fit of the data in both the normal state and the Meissner state using Eqs. (12) and (13) to describe $B(z)$, Eqs. (14) and (15) to parameterize $\rho(z,E)$, and Eq. (16) to convolve the terms into an expression for $\langle B\rangle(E)$ (see Sec. III). The fit quality is excellent, with the model capturing all features of the data. Values obtained for λ are indicated in the inset of each subplot, while the full set of fit parameters is tabulated in Table I.

TABLE I. Fit results for our Nb samples with different surface treatments commonly used to fabricate SRF cavities (see Sec. II B) obtained using the analysis approach described in Sec. III (see also Fig. 3). Here, T is the absolute temperature , B_{applied} is the strength of the magnetic field applied parallel to the sample surface, $\tilde{N}$ is the sample's (effective) demagnetization factor, d is the thickness of the (nonsuperconducting) "dead layer" at the sample surface, and $\lambda(T)$ is the magnetic penetration depth (measured at temperature T). Also included are quantities derived from Eqs. (17)–(19): the magnetic penetration depth at 0 K (λ_0), the carrier mean free path (ℓ), and the "effective" coherence length (ξ_0'). For comparison, we also include values for several Nb/Cu films commonly used in SRF cavities [62] (obtained from a reanalysis of the data using the formalism described in Sec. III) and results for a "clean" Nb/Al_2O_3 film [25]. The abbreviations listed with these samples correspond to direct-current magnetron sputtering (DCMS), high-power impulse magnetron sputtering (HIPIMS), and High-Intensity-and-Energy Isotope Mass Separator Online Device (HIE-ISOLDE). The dependence of λ_0 on ℓ is also shown in Fig. 4.

Sample	T (K)	B_{applied} (mT)	$\tilde{N}$	d (nm)	$\lambda(T)$ (nm)	λ_0 (nm)	ℓ (nm)	ξ_0' (nm)	Reference
Nb (baseline)	2.63	25.11 ± 0.05	0.000 ± 0.027	21.8 ± 0.7	31.3 ± 0.7	31.2 ± 0.7	260 ± 80	34.8 ± 3.0	This work
Nb (120 °C bake)	2.72	25.179 ± 0.034	0.006 ± 0.011	25.4 ± 1.3	42.6 ± 1.3	42.4 ± 1.3	35 ± 5	18.8 ± 1.6	This work
Nb (75 °C + 120 °C bake)	2.69	25.162 ± 0.032	0.000 ± 0.028	18.7 ± 0.6	32.3 ± 0.5	32.2 ± 0.5	175 ± 34	32.8 ± 2.6	This work
Nb (N_2 infusion)	2.83	25.11 ± 0.06	0.009 ± 0.011	24.1 ± 1.6	70.2 ± 2.6	69.9 ± 2.5	8.4 ± 1.0	6.9 ± 0.7	This work
Nb/Cu (DCMS)	3.25	15.14 ± 0.05	0	14.3 ± 1.2	51.1 ± 1.2	50.7 ± 1.2	19.6 ± 2.2	13.2 ± 1.1	[62]
Nb/Cu (HIE-ISOLDE)	2.65	15.010 ± 0.024	0	13.1 ± 0.5	37.8 ± 0.7	37.7 ± 0.7	59 ± 7	23.9 ± 1.7	[62]
Nb/Cu (HIPIMS)	3.75	15.09 ± 0.04	0	17.3 ± 0.6	34.6 ± 0.4	34.1 ± 0.4	106 ± 14	29.2 ± 2.1	[62]
Nb/Al_2O_3 (DCMS)		8.82	0	2 ± 2		27 ± 3	359	36	[25]

Following the above discussion, with our expressions for $B(z)$ [Eqs. (12) and (13)] and $\rho(z,E)$ [Eqs. (14) and (15)] in hand, it is now straightforward to construct an expression for $\langle B\rangle$ that depends on E:

$$\langle B\rangle(E) = \int_0^\infty B(z)\rho(z,E)\,dz, \tag{16}$$

where the dependence on E is accounted for *implictly* by $\rho(z,E)$ [111]. Note that, as described above, $\rho(z,E)$'s "shape" parameters are all *predetermined* from fitting a series of implantation profiles and interpolating their values. Consequently, this "staged" analysis approach [112] uses the *maximum* amount of available information when fitting the data and does not, for example, assume that the average stopping depth, $\langle z\rangle$, is an adequate proxy for the *full* stopping distribution [113]. Therefore, Eq. (16) depends on the main parameters that define the shape of $B(z)$ [Eqs. (12) and (13)]: λ, d, B_{applied}, and $\tilde{N}$. Before proceeding, we point out that the integral in Eq. (16) must be evaluated *numerically*; however, it is found that adaptive Gaussian quadrature routines (see, e.g., Ref. [114]), which are widely available in free scientific software (e.g., the PYTHON package SciPy [115]), are adequate for this task. Fit results for each sample are given in Fig. 3, showing excellent agreement with the data, and the resulting fit parameters are given in Table I.

IV. DISCUSSION

From Fig. 3, it is clear that the different surface treatments affect the Meissner screening profile in Nb within the first 150 nm below its surface. As mentioned in Sec. III, a hierarchy is evident; the applied field is attenuated most strongly in the "baseline" sample, yielding $\lambda = 31.3 \pm 0.7$ nm, followed closely by the "75 °C + 120 °C bake" treatment, where $\lambda = 32.3 \pm 0.5$ nm. In the "120 °C bake" sample, the screening is weakened significantly compared to the previous two treatments, amounting to a magnetic penetration depth of 42.6 ± 1.3 nm. This is diminished even further for the "N_2 infusion" treatment, for which $\lambda = 70.2 \pm 2.6$ nm. The results suggest that further preparation beyond our "baseline" treatment serves to diminish Nb's capacity to prevent magnetic flux from "leaking" below its surface in the Meissner state.

For a closer quantitative comparison between our results, it is first necessary to account for the (minor) temperature differences between measurements (see Fig. 3). For this, we use the well-known "two-fluid" expression [116]

$$\lambda(T) = \frac{\lambda_0}{\sqrt{1-(T/T_c)^4}}, \tag{17}$$

where λ_0 is the magnetic penetration depth at 0 K, to extrapolate the λ values down to absolute zero (see Table I) [117]. Extrapolating to this limit is convenient, since at 0

K we also have the simple relationship [116]

$$\lambda_0 = \lambda_L \sqrt{1 + \frac{\xi_0}{\ell}}, \tag{18}$$

where λ_L is the so-called London penetration depth, ξ_0 is the Pippard [23] or Bardeen-Cooper-Schrieffer [24] coherence length, and ℓ is the carrier mean free path (i.e., the average distance traveled before being scattered). As both λ_L and ξ_0 can be regarded as material properties intrinsic to Nb, differences in λ_0 can be understood in terms of different ℓ values for our samples. By aid of Eq. (18) and literature estimates [118] for both $\lambda_L = 29.01 \pm 0.10$ nm [14,16–18,119–127] and $\xi_0 = 40.3 \pm 3.5$ nm [14,16–18, 119–121,125,127–129], we calculate ℓ for our samples, with the results tabulated in Table I. These values compare well with typical ℓ values found in SRF Nb [130,131]; however, to better understand their differences, we must consider the material modifications introduced by these treatments.

We start with the "baseline," which is simplest case to consider. As described in Sec. II B, this treatment first removes mechanical stresses through annealing and afterwards purges surface imperfections in the topmost material to mitigate any contamination from the furnace. The procedure is highly successful, as evidenced by our measured λ value's close proximity to λ_L, suggesting that the level of impurities is low, corresponding to $\ell = 260 \pm 80$ nm. This is somewhat lower than the $\ell \sim 810$ nm expected for Nb with a residual-resistivity ratio of approximately 300 (see, e.g., Refs. [132,133]); however, we point out that our *microscopic* method of determining ℓ samples only the spatial region probed by the μ^+ beam, making it more sensitive to the surface region, where, for example, interstitial impurities are likely more prevalent. Similarly, it is at first surprising to find that nonlocal electrodynamics [23,24] are not necessary to describe the data; however, this is consistent with our ℓ, which equivalently yields a short "effective" coherence length ξ_0' (at 0 K) according to [116]

$$\frac{1}{\xi_0'} = \frac{1}{\xi_0} + \frac{1}{\ell}. \tag{19}$$

For the "baseline" sample, we get $\xi_0' = 34.8 \pm 3.0$ nm, which is very close to λ_0 and equivalent to $\xi_0'/\lambda_0 = 1.11 \pm 0.10$. Thus, we conclude that this sample is close to the "boundary" where the influence of nonlocal electrodynamics becomes significant, and we anticipate such effects being more prevalent in samples of higher purity [134].

We now consider the "120 °C bake" sample. The main effect of the baking [44] is to "dissolve" some of the surface oxide into the bulk of Nb. This treatment instigated a refinement of the oxygen-transport model in Nb [135] which has received renewed attention lately [136]. Even before the invention of this "recipe," oxygen-diffusion profiles in Nb were of interest for their influence on the surface barrier associated with flux penetration [137]. Consistent with the empirical observation that this mild baking helps mitigate the so-called Q slope observed in SRF cavities at high E_{acc}, we observe a λ_0 appreciably larger than λ_L (equivalent to a reduced supercurrent density at the surface—see, e.g., Ref. [55]), accompanied by $\ell = 35 \pm 5$ nm and $\xi_0' = 18.8 \pm 1.6$ nm. These values are consistent with a sample whose surface region has been "dirtied" by the (intentional) addition of impurities. Interestingly, not only is this ℓ much larger than the values reported for this treatment in another LE-μSR study [53], the Meissner screening profile is also different. While the bipartite behavior reported previously [53] has been suggested to originate from the baking [44] producing an "effective" superconductor-superconductor bilayer [54–56] (i.e., from a thin "dirty" surface on top of a "clean" bulk), no evidence for such behavior is observed here. Separate LE-μSR measurements on *real* bilayers [138] reveal screening profiles that are qualitatively distinct from those reported here (see Fig. 3). Thus, we suggest that low-temperature baking [44] does *not* fundamentally alter the character of Meissner screening in Nb and that the earlier results [53] require an alternative explanation.

Next, we consider the "75 °C + 120 °C bake" sample. Given what is known about mild baking [44], the results for this two-step treatment [45] confound expectations. The similarity of its λ_0 and derived quantities to those from the "baseline" treatment (see Table I) suggests that the "extra" baking time undermines the level of defects near the surface. Explicit investigations into this matter are limited; however, one study using positron-annihilation spectroscopy proposed that the procedure [139] initially causes an increase in the Nb-vacancy concentration through the decomposition of hydride-vacancy complexes, that subsequent annealing at 120 °C gradually removes the complexes by thermally activated release, and that the remaining vacancies are vanquished by diffusion to trapping sites and gradually annealed out. While this mechanism is plausible, it does not consider the dissolution of oxygen from the surface during the second step [44], which should have the *opposite* influence on λ. Thus, we suggest that further investigation into the near-surface chemical composition (e.g., using secondary-ion mass spectrometry) is needed to be conclusive.

Lastly, we consider the remaining surface treatment "N_2 infusion" [47], which is quite different from the other surface treatments. In this "recipe," N_2 gas is intentionally introduced during baking to dope Nb with nitrogen. The "infusion" is performed at the relatively low temperature of 120 °C, which limits the diffusivity of nitrogen [140], but mitigates the requirement of surface removal after the treatment (see the original doping recipe [46]). Given this treatment's substantial dopant "supply" [47] and

nitrogen's diffusivity in Nb (see, e.g., Ref. [140]), it is not surprising that we obtain our greatest λ_0 among all the surface treatments, and, correspondingly, the smallest ℓ and ξ_0'—8.4 ± 1.0 nm and 6.9 ± 0.7 nm, respectively.

Thus, following the above discussion, we propose that the observed hierarchy in λ_0 for the studied surface treatments is readily explained by their propensity to dope Nb's near-surface region. This (relatively light) doping alters ℓ in the spatial region sampled by LE-μSR, resulting in $\lambda_0 > \lambda_L$. This relationship is shown graphically in Fig. 4, accompanied by results from related studies for comparison [25,62]. The results imply that either ℓ is sufficiently homogeneous over the range of μ^+ stopping depths (see Fig. 1) to be encapsulated by a single (average) value or the effect of any inhomogeneity in ℓ is beyond the detection limit of the current measurements. Alternatively, the largest inhomogeneity may be localized very close the surface, comparable to the nonsuperconducting region observed in our samples (see Fig. 3), considered below.

It is not uncommon to find a thin layer at a superconductor's surface that does not screen an external field, colloquially called a "dead layer." One typically accounts for this "feature" by incorporating the *ad hoc* parameter d into models of the screening profile—see Eq. (12). A literature survey suggests that d is a generic feature of superconductors (see, e.g., Refs. [25,53,62,97–103]), indicating that the value is representative of a particular *sample*, rather than being intrinsic to the material. For example, while a "dead layer" on the order of approximately 20 nm is common for SRF Nb [53,62] (which we also obtain here—see Table I), values comparable to the thickness of the (native) surface oxide layer (approximately 5 nm [109]) are found in high-quality epitaxial thin films [25,141]. Some of this variance is likely attributed to differences in surface roughness, which can reduce a sample's screening capacity at the surface [104–106]; however, it alone cannot account for the full extent of d in certain materials, leading us to consider other possibilities.

Recently, several authors have considered the possibility of λ being spatially *inhomogeneous*, resulting from a varying defect-concentration profile close to Nb's surface [142,143]. For a sufficiently high concentration of surface-localized defects, it is plausible that $\lambda(z)$ could become great enough to qualitatively mimic the effect of a "dead layer." Such a scenario has been considered theoretically for $\lim_{z\to 0} \lambda(z) = \infty$ [144], producing a gradual (rather than sharp) transition between nonsuperconducting and superconducting regions. While such an idea is intriguing, our data in Fig. 3 are not refined enough to resolve such features, and further measurements (e.g., with fine E steps below 10 keV) are required to be more conclusive. Such measurements may require a condensed N_2 overlayer, which can be grown *in situ* at the cryogenic temperatures used in the experiments described here (see, e.g., Ref. [62]).

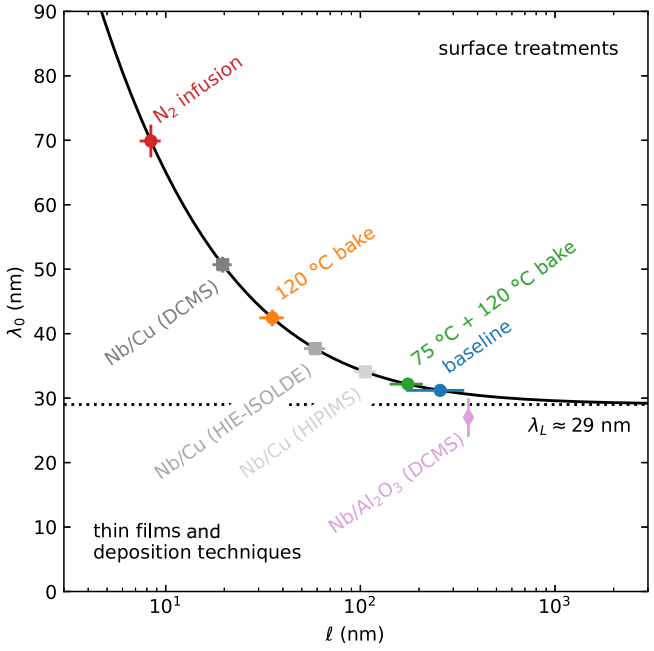

FIG. 4. Dependence of Nb's magnetic penetration depth at 0 K, λ_0, on the carrier mean free path, ℓ, for common surface treatments used to fabricate SRF cavities. The values are calculated according to Eq. (18) (solid black line) using representative values for the London penetration depth $\lambda_L = 29.01 \pm 0.10$ nm [14,16–18,119–127] and the Bardeen-Cooper-Schrieffer coherence length $\xi_0 = 40.3 \pm 3.5$ nm [14,16–18,119–121,125,127–129]. Also included for comparison are values for Nb/Cu films [62] prepared with different techniques (re-evaluated using the approach described in Sec. III), and a very "clean" Nb/Al_2O_3 film [25]. All plotted values derived from this work are tabulated in Table I. DCMS, direct-current magnetron sputtering; HIE-ISOLDE, High-Intensity-and-Energy Isotope Mass Separator Online Device; HIPIMS, high-power impulse magnetron sputtering.

At this juncture, we point out that while our field-screening measurements reported in Sec. III focus exclusively on the direct-current regime, typical SRF cavities operate in alternating-current fields at 5–10 GHz, and our results do not preclude the existence of frequency-dependent effects in our samples. Generally, practical treatments of $B(z)$ and λ take either term as frequency independent; however, verifying this assertion directly in the future with a suitable method of interrogation (e.g., LE-μSR) remains highly desirable.

Finally, it is worth noting that an analysis approach similar to that described in Sec. III has also been used in ^{8}Li β-detected-NMR [57,58] measurements on a Nb thin film [141]. While the β-detected-NMR technique shares many similarities with and is complementary to LE-μSR [145], it has the advantage of being able to operate in (surface-parallel) magnetic fields up to 200 mT [146], covering the operating conditions of SRF cavities and close to Nb's B_{sh} [50,51]. Although equivalent measurements

using LE-μSR are not currently possible, the results presented here provide a good point of comparison for future investigations using β-detected NMR.

V. CONCLUSIONS

Using LE-μSR, we determine the Meissner screening profile in Nb samples that recieved surface treatments commonly used to prepare SRF cavities. In contrast to an earlier report [53], we find no evidence for any "anomalous" modifications to the Meissner profiles, ruling out that low-temperature baking [44], two-step baking [45], or N_2 infusion [47] produces an "effective" bilayer superconductor [54–56]. Instead, we find that the observed field screening is well described by a simple London model [63], with magnetic penetration depths (extrapolated to 0 K) of 31.3 ± 0.7 nm for the "baseline" sample, 42.6 ± 1.3 nm for the "120 °C bake" treatment, 32.3 ± 0.5 nm for the "75 °C + 120 °C bake" recipe, and 70.2 ± 2.6 nm for "N_2 infusion." Differences in screening properties between surface treatments can be explained by changes to the carrier mean free paths resulting from dopant profiles near Nb's surface. A relatively large (approximately-20-nm) nonsuperconducting "dead layer" is found in all samples, exceeding the thickness of the native oxide layer that forms at Nb's surface [109]. This observation may suggest a narrow region near the surface where λ is *depth dependent* [136,142,144]. Further LE-μSR experiments, with finer energy steps where $E < 10$ keV, may illuminate the matter.

ACKNOWLEDGMENTS

We thank P. Kolb, R. E. Laxdal, W. A. MacFarlane, and E. Thoeng for useful discussions, TRIUMF's SRF group for providing several of the Nb samples ("baseline," "120 °C bake," and 75 °C + 120 °C bake"), and M. Martinello for preparing the "N_2 infusion" sample. This work is based on experiments performed at the Swiss Muon Source SμS, Paul Scherrer Institute, Villigen, Switzerland. Financial support was provided by a Natural Sciences and Engineering Research Council of Canada Grant to T. Junginger.

APPENDIX: SIMULATING MUON IMPLANTATION

As is clear from Sec. III, a crucial aspect of our analysis is the inclusion of simulated μ^+ stopping profiles, which serve as the kernel of the integral transform defined in Eq. (16). Given their importance, we now consider some of their details further.

In general, energetic charged particles lose their kinetic energy through the interaction with matter encountered along their trajectory. For a particle penetrating a (solid) target, this happens through a series collisions with the host's electrons and nuclei [147]. In this slowing process, the average energy loss per unit distance is often called the "stopping power":

$$S \equiv -\frac{dE}{dz}, \tag{A1}$$

where E is the energy and z is the position of the projectile. Naturally, S can be thought of as a property specific to a particular projectile-target combination. Typically, S is decomposed into electronic, S_e, and nuclear, S_n, contributions,

$$S = S_n + S_e, \tag{A2}$$

such that these contributions may be treated separately (see below). Practically, it is convenient to *normalize* each S_i by the target's number density, n, converting them into stopping *cross sections*:

$$\tilde{S}_i \equiv \frac{S_i}{n}. \tag{A3}$$

Note that $\tilde{S}_i$ is typically reported in "odd"-looking units (e.g., 10^{-15} eV cm^2 per atom).

As there are an endless number of projectile-target combinations, significant effort has been invested in predicting $\tilde{S}$, which can be used to calculate a projectile's *range* (i.e., its average implantation depth) in *any* target via

$$\langle z \rangle = \int_E^0 \frac{1}{n\tilde{S}}\, dE. \tag{A4}$$

This task, however, is formidable, and no single theoretical formalism dominates to date. Although progress with theory continues to be made (see, e.g., Ref. [148]), a phenomenological treatment of $\tilde{S}_i$ is often used, wherein measured values are parameterized using a semiempirical model. At the implantation energies used in a LE-μSR experiment [59,60], the *electronic* contribution to $\tilde{S}$ has the greatest impact on a muon's range, and we now focus on $\tilde{S}_e$.

One parameterization of $\tilde{S}_e$ that has been used for more than half a century is the so-called Varelas-Biersack formulas [75], which describe the stopping cross section in terms of five coefficients, A_i, within the low-energy implantation regime (1–1000 keV). In this treatment, the energy dependence is expressed in terms of the scaled quantity

$$\tilde{E} \equiv E\left(\frac{u}{m}\right), \tag{A5}$$

where E is the projectile energy (in kiloelectronvolts) and m is its mass (in unified atomic mass units [84]) [149]. For

muons (i.e., light protons), $\tilde{S}_e$ is given by [73–75]

$$\tilde{S}_e = \begin{cases} A_1\sqrt{\tilde{E}}, & 1\ \text{keV} \le \tilde{E} < 10\ \text{keV}, \\ \dfrac{s_{\text{low}}(\tilde{E})\, s_{\text{high}}(\tilde{E})}{s_{\text{low}}(\tilde{E}) + s_{\text{high}}(\tilde{E})}, & 10\ \text{keV} \le \tilde{E} < 1\ \text{MeV}, \end{cases} \tag{A6}$$

where

$$s_{\text{low}}(\tilde{E}) = A_2\tilde{E}^{0.45} \tag{A7}$$

and

$$s_{\text{high}}(\tilde{E}) = \left(\frac{A_3}{\tilde{E}}\right)\ln\left(1 + \frac{A_4}{\tilde{E}} + A_5\tilde{E}\right). \tag{A8}$$

While Eqs. (A6)–(A8) require five A_i's, smooth continuity implies that

$$A_1 \equiv \left(\frac{1}{\sqrt{10\ \text{keV}}}\right)\frac{s_{\text{low}}(10\ \text{keV})\, s_{\text{high}}(10\ \text{keV})}{s_{\text{low}}(10\ \text{keV}) + s_{\text{high}}(10\ \text{keV})},$$

reducing the number of "free" parameters from five to four. Equations (A6)–(A8) have proved to be so useful that several compilations of the A_i's have been made [73,74] for the purpose of facilitating simulations of ion implantation. Important for us, the Monte Carlo code TRIM.SP [70–72] relies on these tabulated values; however, the most-recent compilation [74] is nearly 30 years old, and a major concern is its current validity.

Quite recently, a large database of electronic stopping cross sections (originally compiled by the late H. Paul) was released by the International Atomic Energy Agency [76], greatly facilitating the comparison of experimental data with different models. Using the compilation, we compare different parameterizations of $\tilde{S}_e$ for H isotopes in Nb against available experimental data [77–80] (omitting clear outliers [150]), as shown in Fig. 5. We find that the earlier tabulations [73,74] *overestimate* $\tilde{S}_e$, likely due to lack of available data at their time of publication [151]. In contrast, our fit to the Varelas-Biersack formulas [75] [Eqs. (A6)–(A8)] gives the best agreement with *all* (reliable) experimental data, and we use our new A_i's (listed in Table II) in all TRIM.SP [70–72] simulations of μ^+ implantation [152].

Finally, we conclude this Appendix with some explicit details of the Monte Carlo simulations of μ^+ implantation in our target, Nb_2O_5(5 nm)/Nb, using TRIM.SP [70–72]. In these simulations, the projectile's trajectory is calculated step-by-step with the assumption that its direction changes with each binary (nuclear) collision and that its path remains straight while it is in "free flight." Energy is primarily lost via the (inelastic) electronic contribution to stopping, which is treated independently from the nuclear

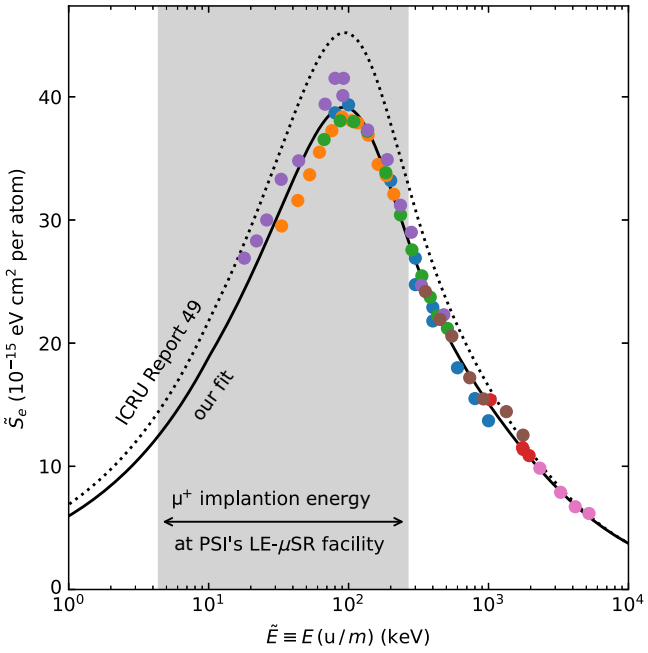

FIG. 5. Electronic stopping cross section, $\tilde{S}_e$, as a function of scaled energy, $\tilde{E}$, for H isotopes implanted in Nb. The filled circles represent measured values, with colors denoting results from different studies [77–80]. The results from one early report [150], which are clear outliers, have been omitted. Different parameterizations of the cross sections using Eqs. (A6)–(A8) (i.e., the Varelas-Biersack formula [75]) are also given, with our fit giving the best agreement with *all* (reliable) experimental data, improving on the older tabulated values [73,74]. The A_i's determined from our fit are listed in Table II. The experimental data were curated by the International Atomic Energy Agency [76]. ICRU, International Commission on Radiation Units & Measurements; PSI, Paul Scherrer Institute.

contribution. The projectile is said to have "come to rest" once its energy drops below a threshold, whereafter its final position is recorded in a histogram, which is output at the end of the simulation. The choices below mainly originate from earlier work that systematically compared μ^+ stopping results against LE-μSR data [69].

Implantation profiles are simulated at select energies, E, between 0.5 and 30 keV. Each simulation uses 10^5 projectiles, whose exact implantation energies are assumed to follow a normal distribution centered at E with a width of 450 eV [153]. Any individual projectiles with $E \le 0$ eV are discarded. The projectile angle of incidence (relative to the surface normal) follows a normal distribution centered at 0° with a width of 15°. A hydrogenlike projectile is assumed, but with the muon's mass, $m_\mu = 0.1134289259(25)$ u [84], which is about one ninth the mass of a proton, $m_p = 1.007276466621(53)$ u [84]. Interactions between the projectile and target atoms are treated using a Molière-type screened Coulomb potential [154] with a Firsov screening length [155]. Interactions between

TABLE II. Values for the A_i's in the (empirical) Varelas-Biersack formula [75]—Eqs. (A6)–(A8)—parameterizing the electronic stopping cross section, $\tilde{S}_e$, for H isotopes implanted in Nb. Plots of Eqs. (A6)–(A8) using the two sets of coefficients, along with all (reliable) experimental data [77–80] from the International Atomic Energy Agency database [76], are shown in Fig. 5. Note that, for brevity, we use SU equivalent to 10^{-15} eV cm^2 per atom when expressing the unit of some of the A_i's.

A_1 (SU keV$^{-1/2}$)	A_2 (SU keV$^{-0.45}$)	A_3 (10^4 SU keV)	A_4 (10^2 keV)	A_5 (10^{-3} keV^{-1})	Ref.
5.96 ± 0.10	6.73 ± 0.08	1.03 ± 0.13	2.8 ± 0.5	3.9 ± 0.9	This work
6.901	7.791	0.9333	4.427	5.587	[73,74]

different target atoms are treated using the so-called Kr-C potential [71,156]. The inelastic energy loss of the μ^+ projectiles is treated using the Varelas-Biersack model [75] [Eqs. (A6)–(A8)] and either tabulated [73,74] or rederived stopping cross sections (see Fig. 5 and Table II). For the target atoms, this is done by using an equipartition of Oen-Robinson (local) [157] and Lindhard-Scharff (nonlocal) [158,159] models. A cutoff energy of 0.5 eV is chosen for the projectiles. Further explanation can be found elsewhere (see, e.g., Ref. [71]). To calculate the stopping power of Nb_2O_5, the so-called Bragg rule is used without any additional "compound" corrections (see, e.g., Ref. [71]). To speed up the simulations, sputtering effects may be omitted (i.e., no recoils are generated). Typical stopping profiles produced from the simulations are shown in Fig. 1.

[1] I. Nowak and M. Ziolek, Niobium compounds: Preparation, characterization, and application in heterogeneous catalysis, Chem. Rev. **99**, 3603 (1999).

[2] J. E. Schlewitz, in *Kirk-Othmer Encyclopedia of Chemical Technology*, Vol. 17 (Wiley, New York, 2009), p. 1, 5th ed.

[3] J. W. Arblaster, The thermodynamic properties of niobium, J. Phase Equilib. Diffus. **38**, 707 (2017).

[4] C. Buzea and K. Robbie, Assembling the puzzle of superconducting elements: A review, Supercond. Sci. Technol. **18**, R1 (2004).

[5] H. A. Leupold and H. A. Boorse, Superconducting and normal specific heats of a single crystal of niobium, Phys. Rev. **134**, A1322 (1964).

[6] G. W. Webb, Low-temperature electrical resistivity of pure niobium, Phys. Rev. **181**, 1127 (1969).

[7] D. P. Karim, J. B. Ketterson, and G. W. Crabtree, A de Haas-van Alphen study of niobium: Fermi surface, cyclotron effective masses, and magnetic breakdown effects, J. Low Temp. Phys. **30**, 389 (1978).

[8] A. Chainani, T. Yokoya, T. Kiss, and S. Shin, Photoemission Spectroscopy of the Strong-Coupling Superconducting Transitions in Lead and Niobium, Phys. Rev. Lett. **85**, 1966 (2000).

[9] L. F. Mattheiss, Electronic structure of niobium and tantalum, Phys. Rev. B **1**, 373 (1970).

[10] G. W. Crabtree, D. H. Dye, D. P. Karim, D. D. Koelling, and J. B. Ketterson, Anisotropic Many-Body Effects in the Quasiparticle Velocity of Nb, Phys. Rev. Lett. **42**, 390 (1979).

[11] F. J. Pinski, P. B. Allen, and W. H. Butler, Calculated electrical and thermal resistivities of Nb and Pb, Phys. Rev. B **23**, 5080 (1981).

[12] R. Blaschke, J. Ashkenazi, O. Pictet, D. D. Koelling, A. T. van Kessel, and F. M. Muller, The influence of band structure on the electromagnetic properties of superconducting Nb and Nb_3Sn, J. Phys. F: Met. Phys. **14**, 175 (1984).

[13] G. W. Crabtree, D. H. Dye, D. P. Karim, S. A. Campbell, and J. B. Ketterson, Anisotropy of the Fermi surface, Fermi velocity, many-body enhancement, and superconducting energy gap in Nb, Phys. Rev. B **35**, 1728 (1987).

[14] H. W. Weber, E. Seidl, C. Laa, E. Schachinger, M. Prohammer, A. Junod, and D. Eckert, Anisotropy effects in superconducting niobium, Phys. Rev. B **44**, 7585 (1991).

[15] J. Neve, B. Sundqvist, and O. Rapp, Electron band structure, resistivity, and the electron-phonon interaction for niobium under pressure, Phys. Rev. B **28**, 629 (1983).

[16] B. W. Maxfield and W. L. McLean, Superconducting penetration depth of niobium, Phys. Rev. **139**, A1515 (1965).

[17] D. K. Finnemore, T. F. Stromberg, and C. A. Swenson, Superconducting properties of high-purity niobium, Phys. Rev. **149**, 231 (1966).

[18] R. A. French, Intrinsic type-2 superconductivity in pure niobium, Cryog. **8**, 301 (1968).

[19] S. B. Nam, Theory of electromagnetic properties of superconducting and normal systems. I, Phys. Rev. **156**, 470 (1967).

[20] S. Y. Savrasov and D. Y. Savrasov, Electron-phonon interactions and related physical properties of metals from linear-response theory, Phys. Rev. B **54**, 16487 (1996).

[21] R. Bauer, A. Schmid, P. Pavone, and D. Strauch, Electron-phonon coupling in the metallic elements Al, Au, Na, and Nb: A first-principles study, Phys. Rev. B **57**, 11276 (1998).

[22] A. Giri, M. V. Tokina, O. V. Prezhdo, and P. E. Hopkins, Electron–phonon coupling and related transport properties of metals and intermetallic alloys from first principles, Mater. Today Phys. **12**, 100175 (2020).

[23] A. B. Pippard, An experimental and theoretical study of the relation between magnetic field and current in a superconductor, Proc. R. Soc. London A **216**, 547 (1953).

[24] J. Bardeen, L. N. Cooper, and J. R. Schrieffer, Theory of superconductivity, Phys. Rev. **108**, 1175 (1957).

[25] A. Suter, E. Morenzoni, N. Garifianov, R. Khasanov, E. Kirk, H. Luetkens, T. Prokscha, and M. Horisberger, Observation of nonexponential magnetic penetration

profiles in the Meissner state: A manifestation of nonlocal effects in superconductors, Phys. Rev. B **72**, 024506 (2005).

[26] A. Maisuradze, A. Yaouanc, R. Khasanov, A. Amato, C. Baines, D. Herlach, R. Henes, P. Keppler, and H. Keller, Evidence for Cooper pair diffraction on the vortex lattice of superconducting niobium, Phys. Rev. B **88**, 140509(R) (2013).

[27] A. Yaouanc, A. Maisuradze, N. Nakai, K. Machida, R. Khasanov, A. Amato, P. K. Biswas, C. Baines, D. Herlach, R. Henes, P. Keppler, and H. Keller, Magnetic field distribution and characteristic fields of the vortex lattice for a clean superconducting niobium sample in an external field applied along a three-fold axis, Phys. Rev. B **89**, 184503 (2014).

[28] T. Reimann, S. Mühlbauer, M. Schulz, B. Betz, A. Kaestner, V. Pipich, P. Böni, and C. Grünzweig, Visualizing the morphology of vortex lattice domains in a bulk type-II superconductor, Nat. Commun. **6**, 8813 (2015).

[29] M. G. Flokstra, S. J. Ray, S. J. Lister, J. Aarts, H. Luetkens, T. Prokscha, A. Suter, E. Morenzoni, and S. L. Lee, Measurement of the spatial extent of inverse proximity in a Py/Nb/Py superconducting trilayer using low-energy muon-spin rotation, Phys. Rev. B **89**, 054510 (2014).

[30] A. Di Bernardo, Z. Salman, X. L. Wang, M. Amado, M. Egilmez, M. G. Flokstra, A. Suter, S. L. Lee, J. H. Zhao, T. Prokscha, E. Morenzoni, M. G. Blamire, J. Linder, and J. W. A. Robinson, Intrinsic Paramagnetic Meissner Effect due to *s*-wave Odd-Frequency Superconductivity, Phys. Rev. X **5**, 041021 (2015).

[31] M. G. Flokstra, N. Satchell, J. Kim, G. Burnell, P. J. Curran, S. J. Bending, J. F. K. Cooper, C. J. Kinane, S. Langridge, A. Isidori, N. Pugach, M. Eschrig, H. Luetkens, A. Suter, T. Prokscha, and S. L. Lee, Remotely induced magnetism in a normal metal using a superconducting spin-valve, Nat. Phys. **12**, 57 (2016).

[32] M. G. Flokstra, R. Stewart, N. Satchell, G. Burnell, H. Luetkens, T. Prokscha, A. Suter, E. Morenzoni, S. Langridge, and S. L. Lee, Observation of Anomalous Meissner Screening in Cu/Nb and Cu/Nb/Co Thin Films, Phys. Rev. Lett. **120**, 247001 (2018).

[33] M. G. Flokstra, R. Stewart, N. Satchell, G. Burnell, H. Luetkens, T. Prokscha, A. Suter, E. Morenzoni, S. Langridge, and S. L. Lee, Manifestation of the electromagnetic proximity effect in superconductor-ferromagnet thin film structures, Appl. Phys. Lett. **115**, 072602 (2019).

[34] R. Stewart, M. G. Flokstra, M. Rogers, N. Satchell, G. Burnell, D. Miller, H. Luetkens, T. Prokscha, A. Suter, E. Morenzoni, and S. L. Lee, Controlling the electromagnetic proximity effect by tuning the mixing between superconducting and ferromagnetic order, Phys. Rev. B **100**, 020505(R) (2019).

[35] J. A. Krieger, A. Pertsova, S. R. Giblin, M. Döbeli, T. Prokscha, C. W. Schneider, A. Suter, T. Hesjedal, A. V. Balatsky, and Z. Salman, Proximity-Induced Odd-Frequency Superconductivity in a Topological Insulator, Phys. Rev. Lett. **125**, 026802 (2020).

[36] M. Rogers, A. Walton, M. G. Flokstra, F. Al Ma'Mari, R. Stewart, S. L. Lee, T. Prokscha, A. J. Caruana, C. J. Kinane, S. Langridge, H. Bradshaw, T. Moorsom, M. Ali, G. Burnell, B. J. Hickey, and O. Cespedes, Spin-singlet to triplet Cooper pair converter interface, Commun. Phys. **4**, 69 (2021).

[37] M. G. Flokstra, R. Stewart, N. Satchell, G. Burnell, H. Luetkens, T. Prokscha, A. Suter, E. Morenzoni, and S. L. Lee, Meissner screening as a probe for inverse superconductor-ferromagnet proximity effects, Phys. Rev. B **104**, L060506 (2021).

[38] H. Alpern, M. Amundsen, R. Hartmann, N. Sukenik, A. Spuri, S. Yochelis, T. Prokscha, V. Gutkin, Y. Anahory, E. Scheer, J. Linder, Z. Salman, O. Millo, Y. Paltiel, and A. Di Bernardo, Unconventional Meissner screening induced by chiral molecules in a conventional superconductor, Phys. Rev. Mater. **5**, 114801 (2021).

[39] G. R. Myneni, Physical and mechanical properties of niobium for SRF science and technology, AIP Conf. Proc. **927**, 41 (2007).

[40] G. Ciovati, P. Dhakal, J. Matalevich, G. Myneni, A. Schmidt, J. Iversen, A. Matheisen, and W. Singer, Mechanical properties of niobium radio-frequency cavities, Mater. Sci. Eng. A **642**, 117 (2015).

[41] H. Padamsee, J. Knobloch, and T. Hays, *RF Superconductivity for Accelerators*, 2nd ed., Wiley Series in Beam Physics and Accelerator Technology (Wiley, New York, 2008).

[42] H. Padamsee, *RF Superconductivity: Science, Technology, and Applications* (Wiley, Weinheim, 2009).

[43] H. Padamsee, 50 years of success for SRF accelerators—a review, Supercond. Sci. Technol. **30**, 053003 (2017).

[44] G. Ciovati, Effect of low-temperature baking on the radio-frequency properties of niobium superconducting cavities for particle accelerators, J. Appl. Phys. **96**, 1591 (2004).

[45] A. Grassellino, A. Romanenko, D. Bice, O. Melnychuk, A. C. Crawford, S. Chandrasekaran, Z. Sung, D. A. Sergatskov, M. Checchin, S. Posen, M. Martinello, and G. Wu, Accelerating fields up to 49MV m^{-1} in TESLA-shape superconducting RF niobium cavities via 75 °C vacuum bake, ArXiv:1806.09824.

[46] A. Grassellino, A. Romanenko, D. Sergatskov, O. Melnychuk, Y. Trenikhina, A. Crawford, A. Rowe, M. Wong, T. Khabiboulline, and F. Barkov, Nitrogen and argon doping of niobium for superconducting radio frequency cavities: A pathway to highly efficient accelerating structures, Supercond. Sci. Technol. **26**, 102001 (2013).

[47] A. Grassellino, A. Romanenko, Y. Trenikhina, M. Checchin, M. Martinello, O. S. Melnychuk, S. Chandrasekaran, D. A. Sergatskov, S. Posen, A. C. Crawford, S. Aderhold, and D. Bice, Unprecedented quality factors at accelerating gradients up to 45 MV m^{-1} in niobium superconducting resonators via low temperature nitrogen infusion, Supercond. Sci. Technol. **30**, 094004 (2017).

[48] C. P. Bean and J. D. Livingston, Surface Barrier in Type-II Superconductors, Phys. Rev. Lett. **12**, 14 (1964).

[49] M. K. Transtrum, G. Catelani, and J. P. Sethna, Superheating field of superconductors within Ginzburg-Landau theory, Phys. Rev. B **83**, 094505 (2011).

[50] T. Junginger, W. Wasserman, and R. E. Laxdal, Superheating in coated niobium, Supercond. Sci. Technol. **30**, 125012 (2017).

[51] T. Junginger, S. H. Abidi, R. D. Maffett, T. Buck, M. H. Dehn, S. Gheidi, R. Kiefl, P. Kolb, D. Storey, E. Thoeng, W. Wasserman, and R. E. Laxdal, Field of first magnetic flux entry and pinning strength of superconductors for rf application measured with muon spin rotation, Phys. Rev. Accel. Beams **21**, 032002 (2018).

[52] D. A. Turner, G. Burt, and T. Junginger, No interface energy barrier and increased surface pinning in low temperature baked niobium, Sci. Rep. **12**, 5522 (2022).

[53] A. Romanenko, A. Grassellino, F. Barkov, A. Suter, Z. Salman, and T. Prokscha, Strong Meissner screening change in superconducting radio frequency cavities due to mild baking, Appl. Phys. Lett. **104**, 072601 (2014).

[54] T. Kubo, Y. Iwashita, and T. Saeki, Radio-frequency electromagnetic field and vortex penetration in multilayered superconductors, Appl. Phys. Lett. **104**, 032603 (2014).

[55] T. Kubo, Multilayer coating for higher accelerating fields in superconducting radio-frequency cavities: A review of theoretical aspects, Supercond. Sci. Technol. **30**, 023001 (2017).

[56] T. Kubo, Optimum multilayer coating of superconducting particle accelerator cavities and effects of thickness dependent material properties of thin films, Jpn. J. Appl. Phys. **58**, 088001 (2019).

[57] W. A. MacFarlane, Implanted-ion βNMR: A new probe for nanoscience, Solid State Nucl. Magn. Reson. **68–69**, 1 (2015).

[58] W. A. MacFarlane, Status and progress of ion-implanted βNMR at TRIUMF, Z. Phys. Chem. **236**, 757 (2022).

[59] P. Bakule and E. Morenzoni, Generation and applications of slow polarized muons, Contemp. Phys. **45**, 203 (2004).

[60] E. Morenzoni, T. Prokscha, A. Suter, H. Luetkens, and R. Khasanov, Nano-scale thin film investigations with slow polarized muons, J. Phys.: Condens. Matter **16**, S4583 (2004).

[61] A. D. Hillier, S. J. Blundell, I. McKenzie, I. Umegaki, L. Shu, J. A. Wright, T. Prokscha, F. Bert, K. Shimomura, A. Berlie, H. Alberto, and I. Watanabe, Muon spin spectroscopy, Nat. Rev. Methods Primers **2**, 4 (2022).

[62] T. Junginger, S. Calatroni, A. Sublet, G. Terenziani, T. Prokscha, Z. Salman, A. Suter, T. Proslier, and J. Zasadzinski, A low energy muon spin rotation and point contact tunneling study of niobium films prepared for superconducting cavities, Supercond. Sci. Technol. **30**, 125013 (2017).

[63] F. London and H. London, The electromagnetic equations of the supraconductor, Proc. R. Soc. London A **149**, 71 (1935).

[64] T. Prokscha, E. Morenzoni, K. Deiters, F. Foroughi, D. George, R. Kobler, A. Suter, and V. Vrankovic, The new μE4 beam at PSI: A hybrid-type large acceptance channel for the generation of a high intensity surface-muon beam, Nucl. Instrum. Methods Phys. Res., Sect. A **595**, 317 (2008).

[65] E. Morenzoni, F. Kottmann, D. Maden, B. Matthias, M. Meyberg, T. Prokscha, T. Wutzke, and U. Zimmermann, Generation of Very Slow Polarized Positive Muons, Phys. Rev. Lett. **72**, 2793 (1994).

[66] T. Prokscha, E. Morenzoni, C. David, A. Hofer, H. Glückler, and L. Scandella, Moderator gratings for the generation of epithermal positive muons, Appl. Surf. Sci. **172**, 235 (2001).

[67] E. Morenzoni, H. Glückler, T. Prokscha, H. P. Weber, E. M. Forgan, T. J. Jackson, H. Luetkens, C. Niedermayer, M. Pleines, M. Birke, A. Hofer, J. Litterst, T. Riseman, and G. Schatz, Low-energy μSR at PSI: Present and future, Phys. B **289–290**, 653 (2000).

[68] Z. Salman, T. Prokscha, P. Keller, E. Morenzoni, H. Saadaoui, K. Sedlak, T. Shiroka, S. Sidorov, A. Suter, V. Vrankovic, and H.-P. Weber, Design and simulation of a spin rotator for longitudinal field measurements in the low energy muons spectrometer, Phys. Proc. **30**, 55 (2012).

[69] E. Morenzoni, H. Glückler, T. Prokscha, R. Khasanov, H. Luetkens, M. Birke, E. M. Forgan, C. Niedermayer, and M. Pleines, Implantation studies of keV positive muons in thin metallic layers, Nucl. Instrum. Methods Phys. Res., Sect. B **192**, 254 (2002).

[70] W. Eckstein and J. Biersack, Sputtering investigations with the Monte Carlo program TRIM.SP, Nucl. Instrum. Methods Phys. Res., Sect. B **2**, 550 (1984).

[71] W. Eckstein, *Computer Simulation of Ion-Solid Interactions*, Springer Series in Materials Science, Vol. 10 (Springer, Berlin, 1991).

[72] W. Eckstein, Backscattering and sputtering with the Monte-Carlo program TRIM.SP, Radiat. Eff. Defects Solids **130–131**, 239 (1994).

[73] H. H. Anderson and J. F. Ziegler, *Hydrogen: Stopping Powers and Ranges in All Elements*, The Stopping and Ranges of Ions in Matter, Vol. 3 (Pergamon Press, New York, 1977).

[74] *Stopping Powers and Ranges for Protons and Alpha Particles*, ICRU Report, Vol. 49 (International Commission on Radiation Units and Measurements, Bethesda, 1993).

[75] C. Varelas and J. Biersack, Reflection of energetic particles from atomic or ionic chains in single crystals, Nucl. Instrum. Methods **79**, 213 (1970).

[76] C. C. Montanari and P. Dimitriou, The IAEA stopping power database, following the trends in stopping power of ions in matter, Nucl. Instrum. Methods Phys. Res., Sect. B **408**, 50 (2017).

[77] E. I. Sirotinin, A. F. Tulinov, V. A. Khodyrev, and V. N. Mizgulin, Proton energy loss in solids, Nucl. Instrum. Methods Phys. Res., Sect. B **4**, 337 (1984).

[78] P. Bauer and D. Semrad, Stopping of hydrogen ions in chemically active metal targets, characterized by AES and RBS, Nucl. Instrum. Methods Phys. Res., Sect. B **13**, 201 (1986).

[79] K. Ogino, T. Kiyosawa, and T. Kiuchi, Stopping powers for MeV tritons in solids, Nucl. Instrum. Methods Phys. Res., Sect. B **33**, 155 (1988).

[80] M. V. Moro, P. Bauer, and D. Primetzhofer, Experimental electronic stopping cross section of transition metals for light ions: Systematics around the stopping maximum, Phys. Rev. A **102**, 022808 (2020).

[81] T. Prokscha, Z. Salman, and A. Suter, in *Muon Spectroscopy: An Introduction*, edited by S. J. Blundell, R. De Renzi, T. Lancaster, and F. L. Pratt (Oxford University Press, Oxford, 2021) Chap. 18, p. 274.

[82] P. A. Zyla, *et al.* (Particle Data Group), Review of particle physics, Prog. Theor. Exp. Phys. **2020**, 083C01 (2020).

[83] A. Yaouanc and P. Dalmas de Réotier, *Muon Spin Rotation, Relaxation, and Resonance: Applications to Condensed Matter*, International Series of Monographs on Physics, Vol. 147 (Oxford University Press, Oxford, 2011).

[84] E. Tiesinga, P. J. Mohr, D. B. Newell, and B. N. Taylor, CODATA recommended values of the fundamental physical constants: 2018, Rev. Mod. Phys. **93**, 025010 (2021).

[85] T. M. Riseman, J. H. Brewer, and D. J. Arseneau, Corrected asymmetry plots, Hyperfine Interact. **87**, 1135 (1994).

[86] G. Ciovati, H. Tian, and S. G. Corcoran, Buffered electrochemical polishing of niobium, J. Appl. Electrochem. **41**, 721 (2011).

[87] C. M. Baglin, Nuclear data sheets for $A = 93$, Nucl. Data Sheets **112**, 1163 (2011).

[88] A. Suter, *The Skewed Gaussian*, Memorandum (Paul Scherrer Institut, Villigen, 2008).

[89] In contrast to the "unusual" definition in Eq. (7), the "conventional" expression for $p_{SG}(B)$ relies on "weighting" $p_G(B)$ via the term in parentheses $[1 + \mathrm{erf}(z)]$ through (positive or negative) values of the parameter ς.

[90] Erfi(z) is usually defined in terms of one of several closely related functions (see, e.g., Ref. [160]). For example, our implementation [88,93] uses the confluent hypergeometric function of the first kind, ${}_1F_1(a, b, z)$, which was made available through the GNU Scientific Library [161] and a "wrapper" within the ROOT framework [95].

[91] A reasonable alternative to this could be to use a sum of $P_G(t)$'s; however, even with only two terms, the sum's degrees of freedom would exceed those of Eqs. (8) and (9).

[92] A detailed account of how using a shared phase ϕ systematically affects the results when one is measuring Meissner screening profiles with LE-μSR can be found elsewhere [162], showing that the effect is minimal in all cases.

[93] A. Suter and B. M. Wojek, Musrfit: A free platform-independent framework for μSR data analysis, Phys. Proc. **30**, 69 (2012).

[94] M. Hatlo, F. James, P. Mato, L. Moneta, M. Winkler, and A. Zsenei, Developments of mathematical software libraries for the LHC experiments, IEEE Trans. Nucl. Sci. **52**, 2818 (2005).

[95] R. Brun and F. Rademakers, ROOT — an object oriented data analysis framework, Nucl. Instrum. Methods Phys. Res., Sect. A **389**, 81 (1997).

[96] One can also use integral reconstruction to deduce $B(z)$ (see, e.g., Refs. [25,60,98]); however, the approach relies on a fast Fourier transform of the "raw" LE-μSR data, making it numerically ill-posed.

[97] T. J. Jackson, T. M. Riseman, E. M. Forgan, H. Glückler, T. Prokscha, E. Morenzoni, M. Pleines, C. Niedermayer, G. Schatz, H. Luetkens, and J. Litterst, Depth-Resolved Profile of the Magnetic Field Beneath the Surface of a Superconductor with a Few nm Resolution, Phys. Rev. Lett. **84**, 4958 (2000).

[98] A. Suter, E. Morenzoni, R. Khasanov, H. Luetkens, T. Prokscha, and N. Garifianov, Direct Observation of Nonlocal Effects in a Superconductor, Phys. Rev. Lett. **92**, 087001 (2004).

[99] R. F. Kiefl, M. D. Hossain, B. M. Wojek, S. R. Dunsiger, G. D. Morris, T. Prokscha, Z. Salman, J. Baglo, D. A. Bonn, R. Liang, W. N. Hardy, A. Suter, and E. Morenzoni, Direct measurement of the london penetration depth in $YBa_2Cu_3O_{6.92}$ using low-energy μSR, Phys. Rev. B **81**, 180502(R) (2010).

[100] O. Ofer, J. C. Baglo, M. D. Hossain, R. F. Kiefl, W. N. Hardy, A. Thaler, H. Kim, M. A. Tanatar, P. C. Canfield, R. Prozorov, G. M. Luke, E. Morenzoni, H. Saadaoui, A. Suter, T. Prokscha, B. M. Wojek, and Z. Salman, Absolute value and temperature dependence of the magnetic penetration depth in $Ba(Co_{0.074}Fe_{0.926})_2As_2$, Phys. Rev. B **85**, 060506(R) (2012).

[101] V. Kozhevnikov, A. Suter, H. Fritzsche, V. Gladilin, A. Volodin, T. Moorkens, M. Trekels, J. Cuppens, B. M. Wojek, T. Prokscha, E. Morenzoni, G. J. Nieuwenhuys, M. J. Van Bael, K. Temst, C. Van Haesendonck, and J. O. Indekeu, Nonlocal effect and dimensions of Cooper pairs measured by low-energy muons and polarized neutrons in type-I superconductors, Phys. Rev. B **87**, 104508 (2013).

[102] E. Stilp, A. Suter, T. Prokscha, Z. Salman, E. Morenzoni, H. Keller, C. Katzer, F. Schmidl, and M. Döbeli, Modifications of the Meissner screening profile in $YBa_2Cu_3O_{7-\delta}$ thin films by gold nanoparticles, Phys. Rev. B **89**, 020510(R) (2014).

[103] L. Howald, E. Stilp, F. Baiutti, C. Dietl, F. Wrobel, G. Logvenov, T. Prokscha, Z. Salman, N. Wooding, D. Pavuna, H. Keller, and A. Suter, Unexpected effects of thickness and strain on superconductivity and magnetism in optimally doped $La_{1.84}Sr_{0.16}CuO_4$ thin films, Phys. Rev. B **97**, 094514 (2018).

[104] M. Lindstrom, B. Wetton, and R. Kiefl, Modelling the effects of surface roughness on superconductors, Phys. Proc. **30**, 249 (2012).

[105] M. Lindstrom, B. Wetton, and R. Kiefl, Mathematical modelling of the effect of surface roughness on magnetic field profiles in type II superconductors, J. Eng. Math. **85**, 149 (2014).

[106] M. Lindstrom, A. C. Y. Fang, and R. F. Kiefl, Effect of surface roughness on the magnetic field profile in the Meissner state of a superconductor, J. Supercond. Novel Magn. **29**, 1499 (2016).

[107] R. Prozorov and V. G. Kogan, Effective Demagnetizing Factors of Diamagnetic Samples of Various Shapes, Phys. Rev. Appl. **10**, 014030 (2018).

[108] E. H. Brandt, Superconductors in realistic geometries: geometric edge barrier versus pinning, Phys. C **332**, 99 (2000).

[109] J. Halbritter, On the oxidation and on the superconductivity of niobium, Appl. Phys. A **43**, 1 (1987).

[110] A. K. Gupta, S. Nadarajah, eds., *Handbook of Beta Distribution and Its Applications* (CRC Press, Boca Raton, 2004).

[111] Formally, Eq. (16) is the integral transform of $B(z)$ by the *kernel* $\rho(z, E)$, wherein $B(z)$ is "mapped" from z space to $\langle B \rangle(E)$ in E space (see, e.g., Ref. [163]).

[112] By "staged analysis approach," we mean that the fitting of the raw LE-μSR data and the fitting of the derived screening profile are done separately. We find that this approach has a pragmatic advantage over more-"direct" approaches [e.g., directly fitting the raw spin-precession signals to a model $B(z)$ through an integral transform analogous to Eq. (16)] in that each assumption or approximation can be performed and verified independently. We note that the correct application of both methods should, of course, yield identical results.

[113] As noted elsewhere [25], using $\langle z \rangle$ can influence the apparent "curvature" in the trend of $\langle B \rangle$, presumably because the mapping from E to $\langle z \rangle$ is nonlinear (see, e.g., Fig. 3).

[114] R. Piessens, E. de Doncker-Kapenga, C. W. Überhuber, and D. K. Kahaner, *QUADPACK: A Subroutine Package for Automatic Integration*, Springer Series in Computational Mathematics, Vol. 1 (Springer, Berlin, 1983).

[115] P. Virtanen, *et al.*, (SciPy 1.0 Contributors), SciPy 1.0: fundamental algorithms for scientific computing in Python, Nat. Methods **17**, 261 (2020).

[116] M. Tinkham, *Introduction to Superconductivity*, 2nd ed., International Series in Pure and Applied Physics (McGraw-Hill, New York, 1996).

[117] Note that T_c is essentially identical for all surface treatments used here (see, e.g., Ref. [52]).

[118] For λ_L, we use a weighted average, correcting for temperature differences using Eq. (17). For ξ_0, we use a statistical average, as most studies do not give uncertainties for their estimates.

[119] J. Auer and H. Ullmaier, Magnetic behavior of type-II superconductors with small Ginzburg-Landau parameters, Phys. Rev. B **7**, 136 (1973).

[120] C. Varmazis and M. Strongin, Inductive transition of niobium and tantalum in the 10-MHz range. I. Zero-field superconducting penetration depth, Phys. Rev. B **10**, 1885 (1974).

[121] P. W. Epperlein, Magnetic penetration depths in superconducting Nb films, Phys. B+C **108**, 931 (1981).

[122] G. P. Felcher, R. T. Kampwirth, K. E. Gray, and R. Felici, Polarized-Neutron Reflections: A New Technique Used To Measure the Magnetic Field Penetration Depth in Superconducting Niobium, Phys. Rev. Lett. **52**, 1539 (1984).

[123] D. A. Korneev, L. P. Chernenko, A. V. Petrenko, N. I. Balalykin, and A. V. Skripnik, in *Neutron Optical Devices and Applications*, Proceedings of SPIE, Vol. 1738, edited by C. F. Majkrzak and J. L. Wood (SPIE, Bellingham, 1992).

[124] D. H. Kim, K. E. Gray, J. D. Hettinger, J. H. Kang, and S. S. Choi, Resistive measurement of the temperature dependence of the penetration depth of Nb in Nb/AlO_x/Nb Josephson junctions, J. Appl. Phys. **75**, 8163 (1994).

[125] A. Andreone, A. Cassinese, M. Iavarone, R. Vaglio, I. I. Kulik, and V. Palmieri, Relation between normal-state and superconductive properties of niobium sputtered films, Phys. Rev. B **52**, 4473 (1995).

[126] H. Zhang, J. W. Lynn, C. F. Majkrzak, S. K. Satija, J. H. Kang, and X. D. Wu, Measurements of magnetic screening lengths in superconducting Nb thin films by polarized neutron reflectometry, Phys. Rev. B **52**, 10395 (1995).

[127] A. V. Pronin, M. Dressel, A. Pimenov, A. Loidl, I. V. Roshchin, and L. H. Greene, Direct observation of the superconducting energy gap developing in the conductivity spectra of niobium, Phys. Rev. B **57**, 14416 (1998).

[128] R. J. Donnelly, in *Physics Vade Mecum*, edited by H. L. Anderson (American Institute of Physics, New York, 1981), p. 118.

[129] K. S. Wood and D. van Vechten, Superconducting detectors for photon and particle spectroscopy: Criteria for transitions to normal state, Nucl. Instrum. Methods Phys. Res., Sect. A **314**, 86 (1992).

[130] S. Casalbuoni, E. Knabbe, J. Kötzler, L. Lilje, L. von Sawilski, P. Schmüser, and B. Steffen, Surface superconductivity in niobium for superconducting RF cavities, Nucl. Instrum. Methods Phys. Res., Sect. A **538**, 45 (2005).

[131] M. Martinello, A. Grassellino, M. Checchin, A. Romanenko, O. Melnychuk, D. A. Sergatskov, S. Posen, and J. F. Zasadzinski, Effect of interstitial impurities on the field dependent microwave surface resistance of niobium, Appl. Phys. Lett. **109**, 062601 (2016).

[132] B. B. Goodman and G. Kuhn, Influence des défauts étendus sur les propriétés supraconductrices du niobium, J. Phys. France **29**, 240 (1968).

[133] E. L. Garwin and M. Rabinowitz, Resistivity ratio of niobium superconducting cavities, Appl. Phys. Lett. **20**, 154 (1972).

[134] While Nb is generally considered a type-II superconductor, we point out that it is very close to the type I–type II boundary, with type-I superconductors being known for their strong nonlocal electrodynamics. It was recently suggested that "clean" Nb is *intrinsically* a type-I superconductor [164] but that (ever-present) disorder and impurities in "real" samples lead to its type-II behavior.

[135] G. Ciovati, Improved oxygen diffusion model to explain the effect of low-temperature baking on high field losses in niobium superconducting cavities, Appl. Phys. Lett. **89**, 022507 (2006).

[136] E. M. Lechner, J. W. Angle, F. A. Stevie, M. J. Kelley, C. E. Reece, and A. D. Palczewski, RF surface resistance tuning of superconducting niobium via thermal diffusion of native oxide, Appl. Phys. Lett. **119**, 082601 (2021).

[137] G. P. van der Mey, P. H. Kes, and D. de Klerk, Influence of oxygen diffusion profiles on the surface barrier of superconducting niobium, Phys. B+C **95**, 369 (1978).

[138] M. Asaduzzaman, *et al.*, unpublished.

[139] M. Wenskat, J. Čižek, M. O. Liedke, M. Butterling, C. Bate, P. Haušild, E. Hirschmann, A. Wagner, and H. Weise, Vacancy-hydrogen interaction in niobium during low-temperature baking, Sci. Rep. **10**, 8300 (2020).

[140] P. Dhakal, Nitrogen doping and infusion in SRF cavities: A review, Phys. Open **5**, 100034 (2020).

[141] R. M. L. McFadden, M. Asaduzzaman, T. J. Buck, D. L. Cortie, M. H. Dehn, S. R. Dunsiger, C. D. P. Levy, G. D. Morris, M. R. Pearson, E. Thoeng, R. F. Kiefl, R. E. Laxdal, W. A. MacFarlane, and T. Junginger, Depth-resolved Meissner screening in a niobium thin film from the spin-lattice relaxation of the implanted β-emitter ^{8}Li, ArXiv:2212.01137.

[142] V. Ngampruetikorn and J. A. Sauls, Effect of inhomogeneous surface disorder on the superheating field of superconducting RF cavities, Phys. Rev. Res. **1**, 012015(R) (2019).

[143] M. Checchin and A. Grassellino, High-field Q-slope mitigation due to impurity profile in superconducting radio-frequency cavities, Appl. Phys. Lett. **117**, 032601 (2020).

[144] Y. S. Barash, The magnetic penetration depth influenced by the proximity to the surface, J. Phys.: Condens. Matter **26**, 045702 (2014).

[145] R. F. Kiefl, G. D. Morris, P. Amaudruz, R. Baartman, J. Behr, J. H. Brewer, J. Chakhalian, S. Daviel, J. Doornbos, S. Dunsiger, S. R. Kreitzman, T. Kuo, C. D. P. Levy, R. Miller, M. Olivo, R. Poutissou, G. W. Wight, and A. Zelenski, Complementarity of low-energy spin polarized radioactive nuclei and muons, Phys. B **289–290**, 640 (2000).

[146] E. Thoeng, R. M. L. McFadden, S. Saminathan, G. D. Morris, P. Kolb, B. Matheson, M. Asaduzzaman, R. Baartman, S. R. Dunsiger, D. Fujimoto, T. Junginger, V. L. Karner, S. Kiy, R. Li, M. Stachura, J. O. Ticknor, R. F. Kiefl, W. A. MacFarlane, and R. E. Laxdal, A new high parallel-field spectrometer at TRIUMF's β-NMR facility, Rev. Sci. Instrum. **94**, 023305 (2023).

[147] Radiative processes (e.g., bremsstrahlung) are also important at high projectile energies; however, for the energies used in LE-μSR, they are unimportant, and we do not consider them further.

[148] A. Schinner and P. Sigmund, Expanded PASS stopping code, Nucl. Instrum. Methods Phys. Res., Sect. B **460**, 19 (2019).

[149] The inclusion of u [84] in Eq. (A5) keeps the "scaling" factor dimensionless [74]; however, the approach is not adopted by all authors [73].

[150] R. Behrisch and B. M. U. Scherzer, Rutherford backscattering as a tool to determine electronic stopping powers in solids, Thin Solid Films **19**, 247 (1973).

[151] Consequently, it is likely that the μ^+ range in Nb (or Nb layers) was *underestimated* in earlier simulations (see, e.g., Refs. [25,29–38,53,62]).

[152] A similar check is also performed for H isotopes implanted in O_2; however, no meaningful deviation from the earlier tabulations [73,74] is found.

[153] The finite width of the distribution is used to account for the spread in energies of the μ^+ eluted from the cryocrystal moderator [66] and the straggling introduced by passage through the carbon-foil detector [165].

[154] G. Molière, Theorie der Streuung schneller geladener Teilchen I. Einzelstreuung am abgeschirmten Coulomb-Feld, Z. Naturforsch. A **2**, 133 (1947).

[155] O. B. Firsov, Calculation of the interaction potential of atoms, Sov. Phys. — JETP **6**, 534 (1958).

[156] W. D. Wilson, L. G. Haggmark, and J. P. Biersack, Calculations of nuclear stopping, ranges, and straggling in the low-energy region, Phys. Rev. B **15**, 2458 (1977).

[157] O. S. Oen and M. T. Robinson, Computer studies of the reflection of light ions from solids, Nucl. Instrum. Methods **132**, 647 (1976).

[158] J. Lindhard and M. Scharff, Energy dissipation by ions in the keV region, Phys. Rev. **124**, 128 (1961).

[159] J. Lindhard, M. Scharff, and H. E. Shiøtt, Range concepts and heavy ion ranges (notes on atomic collisions, II), Mat. Fys. Medd. Dan. Vid. Selsk. **33**, 14 (1963).

[160] F. W. Olver, D. W. Lozier, R. F. Boisvert, C. W. Clark, eds., *NIST Handbook of Mathematical Functions* (Cambridge University Press, New York, 2010).

[161] M. Galassi, J. Davies, J. Theiler, B. Gough, and G. Jungman, *GNU Scientific Library Reference Manual* (Network Theory Ltd., Surrey, 2009), 3rd ed.

[162] M. M. Hossain, *Absolute value of the magnetic penetration depth and field profile in the Meissner state of exotic superconductors yttrium barium copper oxide and Co-doped pnictide*, Ph.D. thesis, University of British Columbia, Vancouver, BC (2012).

[163] G. B. Arfken and H. J. Weber, *Mathematical Methods for Physicists* (Elsevier, Burlington, 2005), 6th ed.

[164] R. Prozorov, M. Zarea, and J. A. Sauls, Niobium in the clean limit: An intrinsic type-I superconductor, Phys. Rev. B **106**, L180505 (2022).

[165] K. S. Khaw, A. Antognini, P. Crivelli, K. Kirch, E. Morenzoni, Z. Salman, A. Suter, and T. Prokscha, Geant4 simulation of the PSI LEM beam line: energy loss and muonium formation in thin foils and the impact of unmoderated muons on the μSR spectrometer, J. Instrum. **10**, P10025 (2015).